A super-twisting observer for atomic-force reconstruction in a probe microscope

Kaiqiang Zhang[a], Toshiaki Hatano[a], Thang Nguyen[c], Christopher Edwards[c], Guido Herrmann[a], Stuart Burgess[a], Massimo Antognozzi[b], Said Khan[a], Robert Harniman[b], Mervyn Miles[b]

[a]*Department of Mechanical Engineering, University of Bristol, BS8 1TR, UK, (corresponding author at Bristol: G. Herrmann, e-mail: G.Herrmann@bris.ac.uk, Tel.: +44-1173315921)*

[b]*School of Physics & Centre for Nanoscience and Quantum Information, University of Bristol, BS8 1FD, UK*

[c]*College of Engineering, University of Exeter, EX4 4QF, UK, (corresponding author at Exeter: C. Edwards, e-mail: C.Edwards@exeter.ac.uk, Tel.: +44-1392726632)*

Abstract

This paper presents a new methodology employing a super-twisting sliding mode observer to reconstruct un-measureable atomic-forces at nano-Newton precision in a Vertically Oriented Probe Microscope (VOPM). The VOPM senses the deflection of a vertically oriented cantilever, caused by shear-force interaction with a confined water layer above the sample-substrate. The paper describes the development of a model and the subsequent experimental process for computing its parameters. This forms the basis for the design of a super-twisting observer to estimate the unknown shear-forces. The reconstructed force can be decomposed into elastic and viscous components, which are important in biological research.

Keywords: Probe Microscope, Shear Force, Elastic and Dissipative Force, Sliding Mode Control, Super-Twisting Observer

1. Introduction

One of the main advantages of atomic force microscopes (AFM) [1] compared to other high resolution devices is that they can be used in ambient, aqueous and vacuum environments. Consequently, these constitute a useful tool for investigating biological specimens in ambient environments. In

conventional AFMs, a horizontally oriented cantilever interacts with the specimen under investigation and a high resolution image can be generated from measuring the interaction force between the cantilever tip and the sample [1, 2, 3, 4] in either contact [1] or intermittent-contact [2] mode. Motivated to improve the imaging precision, much research [5, 6] has been carried out to resolve various control issues in typical AFMs. Specifically, one shortcoming experienced by traditional AFM systems (i.e. devices with horizontal cantilevers) is the 'snap-to-contact' effect which they experience. This occurs when the attractive atomic forces dominate the inherent stiffness of the cantilever [4, 7] . A *Vertically Oriented Probe microscope* (VOPM) [8, 9, 10, 11, 12, 13, 14, 15] circumvents this difficulty because of its non-standard design. In this arrangement, a shear force between the cantilever tip and a small ordered water layer is exploited for measurement. It increases as the proximity to the specimen increases, and causes a decrease in the oscillation amplitude of the cantilever. Most existing shear force microscopy systems [14, 15] use for actuation a tuning fork, and have a resonance frequency usually below 50 kHz. In contrast, Bristol's VOPMs exploit the higher resonance frequency of the cantilever which are often well above 100 kHz or even above 1 MHz [8, 9, 10, 11]. Such a high resonance frequency permits a higher available detection frequency, and, thus, a high scanning bandwidth of the microscope. The high resonance frequency and small oscillating amplitude of the cantilever require a very sensitive detection system: a scattered evanescent wave (SEW) technique [8], unique to Bristol's VOPMs, has enabled such high sensitivity.

This paper investigates the problem of estimating the shear forces by using an unknown input observer framework. In general, for probe microscopes, the interaction force reconstruction has been recently of great interest to bio-medical scientists to understand sub-cell-biological processes, for instance in cancer treatment [16]. There it was carried out by offline processing the cantilever oscillation or deflection [17, 18, 16]. In contrast, the work in this paper provides a complete protocol for a model-based, fast, in principle, online estimator. The structure of the model which underpins the observer design, with its relative degree two characteristics capturing the dynamics between the unknown force and the tip of the cantilever, suggests the use of a super-twisting observer [19]. It is well known that sliding mode observers exhibit a high degree of accuracy and are capable of simultaneously estimating both the state variables and unknown inputs with finite-time guarantees [19, 20, 21]. This is quite different from the characteristics of high gain ob-

servers [22]. Because of the specific form of the state-space systems which result from the modelling process, the work proposed in [19] is used as the starting point for the approach in this paper and will exploit the fact that the equivalent output injection signal can accurately reconstruct the unknown tip-sample shear force. Subsequently, elastic (cantilever tip-position in-phase) and viscous (out-of-phase) forces can be identified [10] applying a least square approach. This results in a specific understanding of the material properties of the investigated specimen, i.e. elasticity and viscosity, at the scanning point. Knowledge of the material properties in biological specimen can be vital to their understanding, e.g. viral infections [23].

Traditional linear unknown input observer structures are not suitable for this problem because they require relative degree one properties. However, it is possible to design a H^{∞}-robust estimator [24]. As discussed later, such an estimator would be of higher order than a super-twisting observer and also lack the unique advantage of the super-twisting observer, which is finite-time convergence.

Observer ideas have been applied to AFM systems previously. For example, in Besancon *et al.* [25] an observer was used to determine the probe loss areas in images and the unknown forces affecting the dynamics of a cantilever [26]. A linear observer has been used to improve the topography measurement of a standard AFM avoiding height measurement distortions due to resonances. This was permissible as frequencies well below 10 kHz were analysed, requiring only a sampling frequency of 20 kHz [27]. Several papers by Jalili and coworkers [28] have considered sliding mode-like observers for unknown input estimation problems related to traditional AFMs. However, this work is limited to relative degree one formulations (achieved by exploiting measurements of both position and velocity) and so cannot be used here[1]. The work described in this paper is also quite different from the probe/sample interaction force estimation approach based on a two degree of freedom model of a tapping mode AFM described in [29].

In this paper, the vertically oriented cantilever (VOC) is first modelled as a 4th order partial differential equation (PDE). This permits an accurate representation of the effects of the exogenous signals, i.e. the measured excitation signal and the unknown shear force on the measured cantilever tip

[1]The SEW technique only provides position and not velocity information about the cantilever tip.

oscillation. This knowledge is the essential basis for a model-based design of an unknown signal estimator. To simplify this representation, without loosing important details, two (rational) 4th order transfer functions are proposed which are accurate in the region of the first and second flexural modes. The cantilever parameters which appear explicitly in the PDE, directly relate to the parameters in the rational transfer function. These are used to develop a state-space model relating the external excitation and the shear force to measured tip position.

In order, for the cantilever dynamics to be accurately reflected by the above mentioned model, in particular, the internal damping of the cantilever needs to be identified. This has been achieved by a prior frequency response analysis using a swept sine approach. This is done when the cantilever is not affected by the shear forces, i.e. when the cantilever is well above the specimen (outside the ordered water layer) but still close enough to be within the evanescent field for cantilever detection. The cantilever frequency response dynamics, assessed in proximity to the specimen, provides insight into the cantilever interacting with the ordered water layer and is used as the basis for the design and testing of the observer.

There are four main contributions in the work presented in this paper[2], which are:

1. An infinite dimensional transfer function (based on the Euler-Bernoulli beam equation) allows the creation of rational transfer functions (and subsequently ordinary differential equation ODE models) which physically relate to the model parameters of the cantilever, allowing further intuitive model-based work.
2. An experimental protocol is provided which characterizes the cantilever dynamics and the cantilever's interaction with the ordered water layer in terms of the internal damping, facilitating the development and calibration of the mathematical model.
3. The super-twisting observer provides robust estimation and interpretation of the VOPM shear forces, i.e. the tip-sample interaction force.
4. The super-twisting observer provides robust estimation and interpre-

[2]This paper presents a super-twisting observer design for shear-force reconstruction in contrast to previous work [30]. Moreover, a systematic practical engineering procedure is developed and described to model the system dynamics, implement the new observer and identify the interaction shear-force.

tation of the VOPM shear forces, i.e. the tip-sample interaction force and their cantilever tip-position in-phase and out-of-phase components. These are elastic and viscous forces and their parameters, viscosity and elasticity constant, are important material parameters.

These combined techniques extend to all classes of shear force microscopes [8, 9, 10, 11, 12, 13, 14, 15], but they can also help in general probe microscopy analysis, specifically in biomedical sciences and sub-cellular analysis [16].

The paper is organized as follows. Section 2 discusses the problem, describes the practical VOPM setup and introduces the mathematical model of the dynamics of the VOPM cantilever probe. In Section 3, the irrational transfer functions capturing the cantilever dynamics will be presented, which will subsequently be approximated by rational transfer functions using a scheme based on the interpretation of Bode diagrams. In Section 4, a super-twisting observer is constructed from a reduced-order model. Section 5 describes the experimental set-up whilst Section 6 details the experimental process carried out to obtain various frequency responses of the lateral cantilever dynamics and the internal cantilever damping, subsequently used as the basis for calibrating the sensor system. The resulting model parametrization provides the basis for the observer design. Section 7 describes the various implementation results. Finally, Section 8 makes some concluding remarks and suggestions for future work. The appendix summarizes the notation used in this paper.

2. The Vertically Oriented Probe Microscope - Problem formulation

Bristol University's vertically oriented probe microscope (VOPM) housed in the Centre for Nanoscience and Quantum Information at the University of Bristol is shown in Fig. 1.

It consists of two main mechanical parts: the head and the adjustable platform. The adjustable platform acts as a physical support for the head and it also carries a horizontal X-Y stage which holds and translates the specimen. The platform also houses an objective lens directly below the imaged specimen. This lens is part of a complex optical system required to measure the excitation amplitude of the cantilever tip via the SEW technique [8]. The bio-specimen is placed on a transparent quartz cover slip, which is mounted in the centre of a high bandwidth horizontal X-Y translational

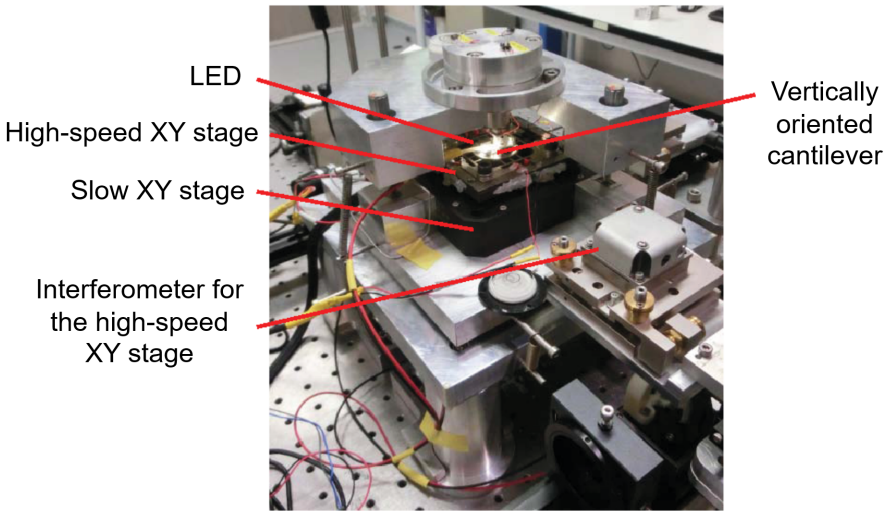

Figure 1: Actual VOPM at the University of Bristol (without heat isolation chamber)

stage. This stage permits the horizontal X- and Y-positioning of the specimen relative to the cantilever in the case of scanning. Fig. 2 shows a schematic diagram of the VOPM detection system.

In Fig. 1 and 2, in the head arrangement, a vertically oriented cantilever (VOC) is extended from the bottom end of an uncoated Si_3N_4 chip (VOC chip)[3]. As the head houses the VOC chip, the two distance measures of the tip of the VOC to the specimen sample and the slide is controlled by vertical piezo-actuators (i.e. oriented as the Z-axis). They are used for precise closed-loop positioning of the cantilever relative to the cover-slip or the specimen sample. The cantilever is sinusoidally excited at its top in the horizontal plane at a frequency close to its first flexural mode by another small piezo actuator operating at an amplitude of around 1 nm (see VOC oscillation direction). Above the coverslip, a light field (the evanescent field in Fig. 2) is created by the complex optical system below the platform to enable the (optical) sensing mechanism developed in [8]. The cantilever tip reflects the scattered laser light of the evanescent field. This reflected laser light is sensed by a photo-detector. As a consequence, the cantilever tip oscillation

[3]The chips are produced by the cantilever vendor, NuNano Ltd., Bristol, UK, www.nunano.com

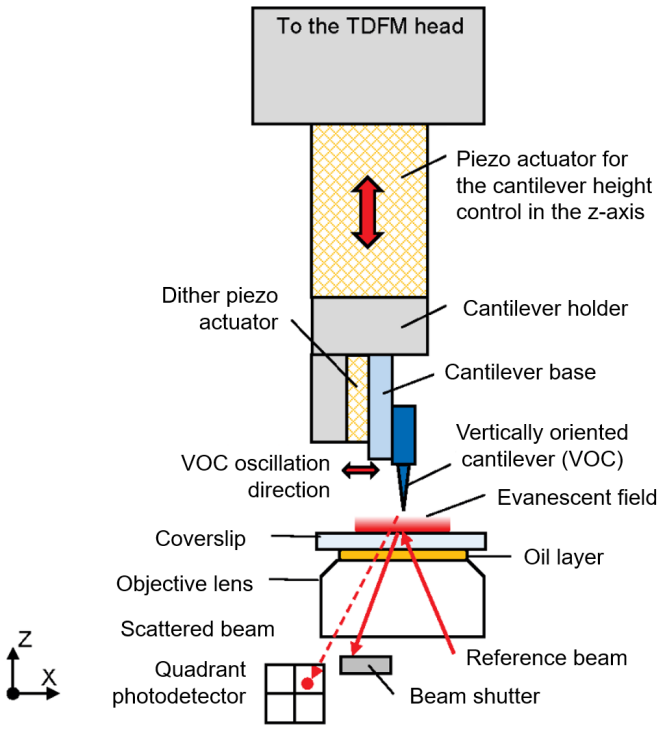

Figure 2: Schematic of the VOPM showing its detection mechanism (including the Vertically Oriented Cantilever (VOC) and VOC chip)

is measured by the reflected optical signal, for details see [8, 9]. Note that the optical system also permits the probe microscope to be simultaneously used as an optical microscope (i.e. the LED in Fig. 1), which assists in the calibration process.

A thin ordered layer of water can be always found on the surface of the specimen (see inset in Fig. 2). This is true for non-biological and biological specimens in ambient conditions (i.e. a normal temperature of 20°C, 101 kPa air pressure and humidity). The ordered layers are about 5 nm thick and are of latice-like structure. Because of the shear force interaction between the cantilever tip and the thin ordered layer of water, the closer the cantilever tip is to the specimen, the higher the shear forces exerted on the tip causing a decrease in the amplitude of oscillation. The VOC has a length of 28 μm, which guarantees that any force occurring within the 5 nm thick layer happens only at the very tip (bottom) of the VOC. Consequently, a measure of the tip-to-specimen distance can be obtained from knowledge of both the

shear force and the oscillation amplitude. Hence, the VOC is modelled here as a beam subject to a known excitation at the top, and a measurable oscillation at the tip (bottom) of the VOC.

Shear Force Estimation problem

The well known Euler-Bernoulli equation from beam theory will be used as the starting point to develop a model of the shear force interaction between the cantilever tip and the specimen [31]. Specifically consider the linear infinite dimensional PDE

$$\frac{\partial^4 EI(Y+\alpha\dot{Y})}{\partial\zeta^4} + \rho A_s \ddot{Y} + \gamma w \dot{Y} = 0 \tag{1}$$

where the boundary conditions are

$$Y(\zeta=0) = u(t) = d_0 \sin(\omega t), \tag{2}$$

$$\frac{\partial Y}{\partial\zeta}(\zeta=0) = 0, \tag{3}$$

$$\frac{\partial^2 Y}{\partial\zeta^2}(\zeta=L) = 0, \tag{4}$$

$$EI\frac{\partial^3 Y}{\partial\zeta^3}(\zeta=L) = -f(t), \tag{5}$$

In equations (1)-(5), α is the internal damping constant, E is Young's modulus, I is the second moment of area, A_s is the cross-sectional area of the cantilever, ρ is its density, γ is the coefficient of damping, L is the length of the cantilever, and its width is denoted by w. The symbol ζ denotes position along the probe axis, while Y represents the transverse displacement at any point along the probe during the oscillation. The quantities $\dot{Y}$ and $\ddot{Y}$ are the first and second derivatives of Y with respect to t and $u(t)$ is the sinusoidal excitation signal of frequency ω and amplitude d_0 applied at the top of the cantilever. In practice, the excitation $u(t)$ is known and represents a sinusoidal input (with a known amplitude d_0 and angular frequency ω) to the dither piezo actuator (see [9]). Because $u(t)$ is the excited displacement occurring at the cantilever's top, the boundary condition $Y|_{\zeta=0}(t) = u(t)$ is enforced in (2) at $\zeta = 0$. Finally, the variable $f(t)$ represents the interaction shear force between the VOC tip and the water layers. This force can be separated into a viscous force and an elastic force according to

$$f(t) = -\nu\frac{\partial Y}{\partial t}\,|_{\zeta=L} - \kappa Y(L) \tag{6}$$

where ν is the constant of dissipative interaction and κ is the elastic interaction constant [31]. The objective is to estimate the unknown shear force signal $f(t)$ in order to better understand and interpret the scan results. In (6), the shear-force interaction is assumed to only occur between the tip of the cantilever and the specimen surface, i.e. $\zeta = L$. Hence, the shear-force and the viscous and elastic parameters, ν and κ, are estimated only at $\zeta = L$ (6). It will be seen in Section 4 that they can be easily separated through a filtered version of $\frac{\partial Y}{\partial t}\,|_{\zeta=L}$ and $\kappa Y(L)$ (6).

3. An ODE-representation from the PDE-beam-model

The linear infinite dimensional model in (1)-(5) provides a direct understanding of how the exogenous signals, the cantilever excitation $u(t)$ and the shear force $f(t)$ influence the cantilever tip position $Y(L,t)$. It is vital to retain this information and yet derive a simplified set of ordinary differential equations for estimation using the super-twisting observer. Hence, by solving the linear infinite dimensional partial differential equation (1) and considering the boundary conditions (2)-(5), it follows (see [32] for more details):

$$Y(L,s) = G_u(L,s)U(s) + G_f(L,s)F(s) \tag{7}$$

where the two transfer functions are

$$G_u(L,s) = \frac{(\cosh(\eta L) + \cos(\eta L))}{\cosh(\eta L)\cos(\eta L) + 1} \tag{8}$$

$$G_f(L,s) = \frac{\cosh(\eta L)\sin(\eta L) - \sinh(\eta L)\cos(\eta L)}{EI\eta^3(\cosh(\eta L)\cos(\eta L) + 1)} \tag{9}$$

and

$$\eta^4 = -\frac{\rho A_s s^2 + \gamma w s}{EI(1+\alpha s)}. \tag{10}$$

In the above, $Y(L,s)$, $U(s)$ and $F(s)$ are the Laplace transforms of $y(L,t)$, $u(t)$ and $f(t)$. Note that $G_u(L,s)$ and $G_f(L,s)$ are computed from the infinite dimensional linear model. Hence, the infinite order is reflected in the numerator and denominator. These functions are locally equivalent to a polynomial of infinite order (see also [33] for some general introduction).

The magnitude components of the Bode diagrams (of the infinite dimensional) transfer functions in (8)-(9) (and their later discussed approximations)

are shown in Fig. 3. For instance, $G_u(L,s)|_{s=0} = 1$ (8) can be observed but also follows from the fact that the cantilever excitation $u(t)$ does not affect any of the resonances so that $u(t) = Y(\zeta = 0, t) = Y(\zeta = L, t)$ for $\omega \to 0$. Hence, these diagrams will be used to help create finite dimensional approximations of (8)-(9).

3.1. Derivation of rational transfer functions

In practise, the cantilever will be excited around the frequency of the first resonance. It is therefore important to obtain a good model in that frequency region providing an accurate gain and phase response match for the low order model from the infinite dimensional model and the measured frequency response close to the resonance. It has therefore been decided to model at best the first two modes of $G_u(L,s)$ and $G_f(L,s)$, thus, creating two rational fourth order transfer functions approximating the ones in Fig. 3 at 'low' frequency. The following rational approximations $\tilde{G}_f(s)$ and $\tilde{G}_u(s)$ to $G_f(L,s)$ and $G_u(L,s)$ are suggested:

$$\tilde{G}_f(s) = \tfrac{L^3}{3EI} H_1(s) H_3(s) \tag{11}$$

$$\tilde{G}_u(s) = H_2(s) H_4(s) \tag{12}$$

where

$$H_1(s) = \frac{w_0^2}{(s^2 + 2\zeta_0 w_0 s + w_0^2)} \tag{13}$$

$$H_2(s) = -\frac{w_0^2 (s + a_0)(s - a_1)}{a_0 a_1 (s^2 + 2\zeta_0 w_0 s + w_0^2)} \tag{14}$$

and

$$H_3(s) = \frac{w_2^2 (s^2 + 2\zeta_1 w_1 s + w_1^2)}{w_1^2 (s^2 + 2\zeta_2 w_2 s + w_2^2)} \tag{15}$$

$$H_4(s) = \frac{-w_2^2 (s + a_2)(s - a_3)}{a_2 a_3 (s^2 + 2\zeta_2 w_2 s + w_2^2)}. \tag{16}$$

In the expressions in (13)-(16), a_i is positive for $i = 0 \ldots 3$ and $w_i > 0$ and $\zeta_i > 0$, for $i = 0 \ldots 2$, represent the natural frequency and damping ratio traditionally associated with 2nd order systems. The four transfer functions, $H_1(s)$, $H_2(s)$, $H_3(s)$ and $H_4(s)$, have at low frequency a gain of one, i.e. $H_1(s)|_{s=0} = H_2(s)|_{s=0} = H_3(s)|_{s=0} = H_4(s)|_{s=0} = 1$. The structure of $\tilde{G}_f(s)$

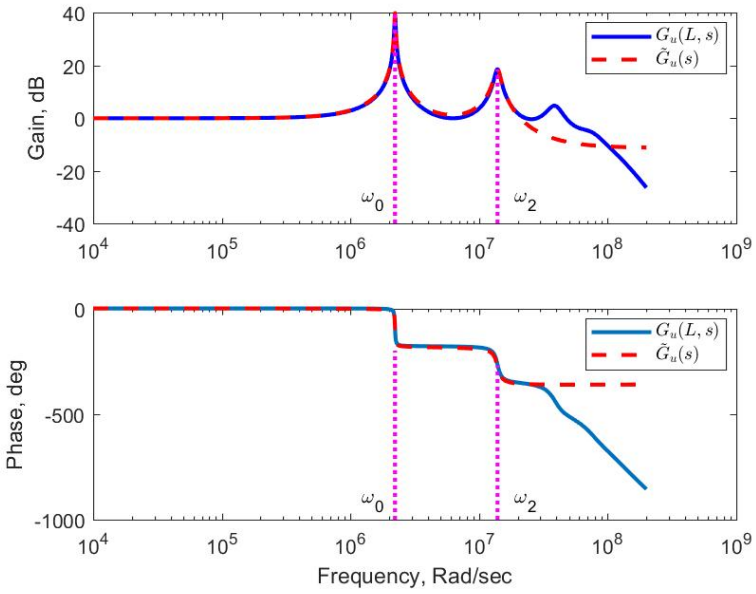

(a)

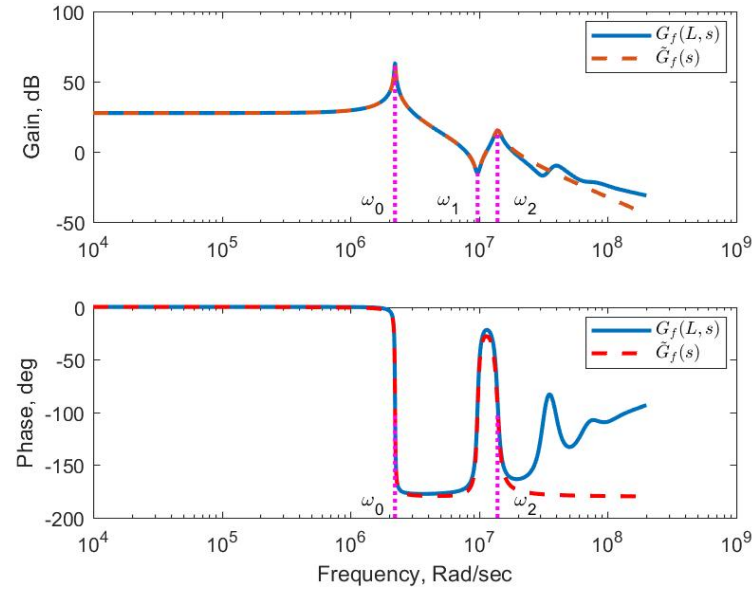

(b)

Figure 3: Bode plots of $G_u(L,s)$ and $G_f(L,s)$ (blue) and their approximation $\tilde{G}_u(L,s)$ and $\tilde{G}_f(L,s)$ (red)

and $\tilde{G}_u(s)$ follows from the Bode diagrams for $G_f(L,s)$ and $G_u(L,s)$ (Fig. 3). Based on both the magnitude and phase plots against frequency (up to a frequency of w_2) suggests an interlaced structure of complex poles (at w_0), followed by a pair of complex zeros (at w_1) and then by a complex pair of poles (w_2). Specifically, an initial peak appears in the magnitude plot at (w_0) and at which frequency there is a sharp drop in phase of -180 °. This is indicative of a complex pair of poles with natural frequency w_0. At frequencies between w_0 and w_1 there is a roll off in magnitude of approximately -40 dBs per decade. At the frequency w_1 there is a sharp trough in the magnitude plot followed by an increase in magnitude of +40 dBs per decade. In terms of phase there is a sharp increase of approximately +180 ° in the region of frequency w_1. This is indicative of a complex pair of zeros with natural frequency w_1. At w_2 a sharp peak appears in the magnitude plot and there is a sharp drop in phase of -180 °. This is indicative of a complex pair of poles with natural frequency w_2. This motivates the model structure for $\tilde{G}_f(s)$.

The model structure for $\tilde{G}_u(s)$ is more subtle. In the Bode diagram for $G_u(L,s)$ (Fig. 3), there are two sharp peaks in the magnitude plot at frequencies of w_0 and w_2 (as for $G_f(L,s)$). Also at these two frequencies there is a drop in phase of -180 °. As before this is indicative of two sets of complex poles with natural frequencies w_0 and w_2. However, in the magnitude plots between the frequencies w_0 and w_2 there is no roll-off at -40 dBs per decade. Also there is no change in phase between these frequencies. This suggests a structure of zeros with configuration $(s+a_0)(s-a_1)$ where $a_0 \approx a_1$. If $w_0 < a_0 < w_2$ then this zero structure provides an increase in magnitude of +40 dBs per decade beyond the break frequency a_0, but with little or no change in phase since $\angle(s+a_0) \approx -\angle(s-a_1)$ (because $a_0 \approx a_1$). Another similar zero structure accounts for the behaviour at frequencies immediately above w_2 preventing the magnitude roll-off immediately following the complex pair of poles with natural frequency w_2. This motivates the model structure for $\tilde{G}_u(s)$.

The model parametrization process will guarantee first the magnitude (and damping) of $G_f(L,s)$ at $s = jw_0$ given through the experimental evaluation of ζ_0 and also the cantilever damping coefficient α. It will be seen that this fully defines $G_f(L,s)$ in (8) and $G_u(L,s)$ in (9). The real zero pair defined by $a_0 > 0$ and $a_1 > 0$ through the choice of $a_0 \approx a_1$ will have minimal effect on phase. Thus, it will allow the adaptation of the magnitude of $\tilde{G}_u(s)$ to $G_u(L,s)$ around the second modal frequency while the phase has been adjusted through the choice of $w_2 > 0$ and $\zeta_2 > 0$. A similar interpretation is

given to $a_2 > 0$ and $a_3 > 0$. Following this justification for the model structures, the subsequent steps will provide detail for process of the parameter computation.

Remark 3.1. *The structure in (14) has nonminimum phase behaviour since one of the zeros lies in the right half-plane. As a direct consequence, this prevents the use of many existing numerical techniques (see for example [34]) for optimally selecting the parameterizing coefficients in (11)-(16).*

As seen later, experimentally, it is difficult to provide comprehensive and complete frequency response details over the whole frequency range of the first two modes. Hence, a mixed approach using knowledge about (8)-(9), (11)-(16), and appropriate experimental results is necessary to obtain a complete set of system parameters.

Establishing the exact value of the frequencies w_i, $i = \{0, 2\}$, requires computing the roots, η_i for $i = \{0, 2\}$, of

$$\cosh(\eta_i L)\cos(\eta_i L) + 1 = 0 \tag{17}$$

which represents the denominator in (8) and (9).

Remark 3.2. *It is well known that (17) has infinitely many solutions. Here η_0 and η_2 denote the two smallest positive solutions.*

Rearranging (10) it follows that

$$\rho A_s s^2 + (\gamma w + \alpha EI\eta_i^4)s + \eta_i^4 EI = 0 \tag{18}$$

from which

$$w_i = \frac{\eta_i^4 EI}{\rho A_s} \tag{19}$$

for $i = \{0, 2\}$. The exact frequency w_1 can be obtained by solving (numerically)

$$\cosh(\eta_1 L)\sin(\eta_1 L) - \sinh(\eta_1 L)\cos(\eta_1 L) = 0 \tag{20}$$

Again the smallest positive solution for η_1, and w_1 is obtained from (19).

Practically, the parameters E, I, A_s, ρ, L, w are usually known. They are provided by the cantilever vendor, here specifically, $E = 210 \cdot 10^9 \frac{kg}{m^{-1}s^{-2}}$, $I = 1.33 \cdot 10^{-27} m^4$, $A_s = 4 \cdot 10^{-13} m^2$, $\rho = 3100 \frac{kg}{m^3}$, $w = 2 \cdot 10^{-6} m$ and $L = 2.8 \cdot 10^{-5} m$, which will be discussed again later in Section 5. It is often

also possible to know either α or γ (here $\gamma = 0$ in air). Practically, α is often unknown and obtained from ζ_0 in Section 6.3. It will be seen that ζ_0 can be obtained through experimental analysis of the gradient of the practically measured phase response $\angle G_u(\cdot)$ (see Section 6.3).

With ζ_0 determined, ζ_1, ζ_2 and the numerator parameters a_0, a_1, a_2 and a_3 are still to be computed. First, assume that

$$H_3(s)|_{s=jw_0} \approx 1 \quad \text{and} \quad H_4(s)|_{s=jw_0} \approx 1, \tag{21}$$

which is feasible for $a_2,\ a_3 >> w_0$ and $w_1,\ w_2 >> w_0$. Then from equation (11), $\tilde{G}_f(jw_0) \approx \frac{L^3}{3EI} H_1(jw_0)$ and from (11) and (13)

$$|G_f(L, jw_0)| = \frac{L^3}{6EI\zeta_0} \tag{22}$$

This can be achieved by adjusting α, which affects the magnitude $|G_f(L, jw_0)|$ in (9), so that (22) is satisfied. This now also defines the magnitude of $|G_u(L, jw_0)|$ in (8).

Assuming as before $H_4(s)|_{s=jw_0} \approx 1$, and then assuming $\angle(s + a_0)(s - a_1)|_{s=jw_0} \approx 0$, which can be achieved if $a_0 \approx a_1$, the two remaining coefficients of $H_2(s)$ can be calculated uniquely by forcing

$$G_u(L, jw_0) = H_2(jw_0) \tag{23}$$

Equation (23) yields two independent equations in two unknowns (a_0 and a_1). Consequently the transfer function $H_2(s)$ is completely specified. Practically, it is now necessary that the experimentally measured magnitude of $\tilde{G}_u(jw_0)$ is calibrated so that it has the now computed magnitude of $|G_u(L, jw_0)|$ at the frequency point at w_0.

Next, ζ_1 and ζ_2 are computed from (11)-(12) which is evaluated at $s = j\omega_1$, and $s = j\omega_2$. Finally the remaining coefficients a_2 and a_3 are obtained from (12) by forcing

$$G_u(L, jw_2) = H_2(jw_2)H_4(jw_2) \tag{24}$$

which yields two equations for the remaining two unknowns a_2 and a_3. A frequency domain comparison between the infinite dimensional transfer functions from (8) and (9) and their approximations in (11)-(12) is shown in Fig. 3.

4. The super-twisting observer

It is clear from the expression for (the approximation of) $\tilde{G}_f(s)$ in (11), (13) and (15) that the relationship between the measurement y and the unknown shear force f is relative degree two. The objective[4] is to estimate f from knowledge of y. A generic state-space representation of the transfer functions in (11) and (12) is

$$\dot{\boldsymbol{x}}(t) = A\boldsymbol{x}(t) + B_u\tilde{u}(t) + B_f\tilde{f}(t) \tag{25}$$

$$y(t) = C\boldsymbol{x}(t) + D\tilde{u}(t) \tag{26}$$

where $A \in \mathbf{R}^{2\times 2}, B_u \in \mathbf{R}^2, B_f \in \mathbf{R}^2$ and the output distribution matrices $C \in \mathbf{R}^{1\times 2}$ and $D \in \mathbf{R}$. Here the second order dynamics of (25)-(26) represent the common first mode identified by w_0. The signals $\tilde{u}$ and $\tilde{f}$ are filtered versions of the sinusoidal input and the shear force respectively and are given by

$$\tilde{u} = H_4(s)u \quad \text{and} \quad \tilde{f} = H_3(s)f \tag{27}$$

where the 'filters' are the stable transfer functions $H_3(s)$ and $H_4(s)$ in (15)-(16). One particular realization, in observable canonical form, is

$$\dot{\boldsymbol{x}}(t) = \begin{bmatrix} -2\zeta_0 w_0 & 1 \\ -w_0^2 & 0 \end{bmatrix} \boldsymbol{x}(t) + \begin{bmatrix} \tilde{b}_1 \\ \tilde{b}_2 \end{bmatrix} \tilde{u}(t) + \begin{bmatrix} 0 \\ \frac{L^3 w_0^2}{3EI} \end{bmatrix} \tilde{f}(t) \tag{28}$$

$$y(t) = \begin{bmatrix} 1 & 0 \end{bmatrix} \boldsymbol{x}(t) - \frac{w_0^2}{a_0 a_1}\tilde{u}(t) \tag{29}$$

where the coefficients

$$\tilde{b}_1 = -\frac{w_0^2}{a_0 a_1}(a_0 - a_1 - 2\zeta_0 w_0) \tag{30}$$

$$\tilde{b}_2 = \frac{w_0^2}{a_0 a_1}(a_0 a_1 + w_0^2). \tag{31}$$

In system (28)-(29), the signals $\tilde{y}$ and $\tilde{u}$ are known but the shear force acting at the tip, $\tilde{f}$, is unknown. With the use of the observable canonical form realization, the unknown state, $\boldsymbol{x}$, does not have a physical representation.

[4]The setting is similar to the approach of Jalili except that in [28] both position and velocity (y and $\dot{y}$) are assumed to be available, and hence traditional relative degree one approaches can be adopted.

The objective is now to estimate $\tilde{f}$ from using only the measured information $\tilde{y}$ and $\tilde{u}$. This represents an unknown input observer problem with the added constraint that the unknown input itself is to be estimated. Note that linear unknown input formations – for example [35, 36] – cannot be directly applied in this situation because they require a relative degree one condition between the measured output and the unknown input. Here, because $CB_f = 0$, this condition is not fulfilled. Instead a sliding mode approach will be adopted. Sliding mode observers exhibit a high degree of accuracy and are capable of simultaneously estimating both the state variables and unknown inputs [19, 20, 21]. Because the system (A, B_f, C), representing the input-output behaviour from the unknown $\tilde{f}$ to measured output $\tilde{y}$, is second order and relative degree two, a super-twisting observer [19, 37] will be employed: Specifically consider the dynamical system

$$\begin{aligned}
\dot{\hat{x}}_1(t) &= -k_1|e_1|^{1/2}\text{sign}(e_1) + \hat{x}_2(t) - 2\zeta_0 w_0 y(t) + \tilde{b}_1\tilde{u}(t) && (32)\\
\dot{\hat{x}}_2(t) &= -k_2\text{sign}(e_1) - w_0^2 y(t) + \tilde{b}_2\tilde{u}(t) && (33)\\
\hat{y}(t) &= \begin{bmatrix} 1 & 0 \end{bmatrix}\hat{\boldsymbol{x}}(t) - \frac{w_0^2}{a_0 a_1}\tilde{u}(t) && (34)
\end{aligned}$$

where k_1 and k_2 are design gains and $e_1(t) = \hat{y}(t) - y(t)$ is the output estimation error. $\dot{\hat{\boldsymbol{x}}} = [\dot{\hat{x}}_1 \quad \dot{\hat{x}}_2]^T$ is the derivative of the estimated state $\hat{\boldsymbol{x}} = [\hat{x}_1 \quad \hat{x}_2]^T$ and $\hat{y}$ is the estimated measurement. Choosing $e_1 = \hat{x}_1(t) - x_1(t)$ and $e_2(t) = \hat{x}_2(t) - x_2(t)$ then the error dynamics satisfy

$$\begin{aligned}
\dot{e}_1(t) &= -k_1|e_1(t)|^{1/2}\text{sign}(e_1(t)) + e_2(t) && (35)\\
\dot{e}_2(t) &= -\underbrace{k_2\text{sign}(e_1(t))}_{v(t)} - \frac{L^3 w_0^2}{3EI}\tilde{f}(t) && (36)
\end{aligned}$$

Here the parameters k_1, k_2 are chosen as in [19, 37] and in particular here

$$k_2 > \frac{L^3 w_0^2}{3EI}\max|\tilde{f}(t)| \tag{37}$$

A practical approach to tune k_1 and k_2 offline is detailed in Section 6.4. During sliding, both $\dot{e}_1 \equiv e_1 \equiv 0$ and from (35) $e_2 \equiv 0$ [37]. Consequently

$$-k_2\text{sign}(e_1(t))\Big|_{eq} - \frac{L^3 w_0^2}{3EI}\tilde{f}(t) = 0 \tag{38}$$

where $\text{sign}(e_1(t))\big|_{eq}$ represents the equivalent injection necessary to maintain sliding [38]. The equivalent injection is the 'average' behaviour of the discontinuous signal $v(t)$ and can be extracted by low-pass filtering of $v(t)$ [38]. Here, a first order low pass filter has been used

$$\tau\dot{\bar{v}}(t) = -\bar{v}(t) + v(t), \quad \tau > 0,\ \bar{v}(0) = 0. \tag{39}$$

and so for a sufficiently small value of τ, it follows that

$$\bar{v} \approx v_{eq} \to -\frac{L^3 w_0^2}{3EI}\tilde{f}$$

Notice from (27) that $f(t) = H_3^{-1}(s)\tilde{f}$ since $H_3(s)$ is bi-proper. Consequently, using the observer (and $H_3^{-1}(s)$), the shear force $f(t)$ can be estimated as $\hat{f}(t)$ in real time:

$$\hat{f} = -\frac{3EI}{L^3 w_0^2}\bar{v}(t) \tag{40}$$

In fact since the poles of $H_3^{-1}(s)$ are almost a decade away in terms of frequency from the modal frequency, $H_3^{-1}(s)$ has been replaced by its DC gain (in this case unity).

Another indication of changes in the tip-to-specimen surface distance can be noted from changes in the shear force model parameters κ and ν in (6). Since $f(t)$ is estimated in real time, the equation (6) can be used to estimate $\kappa(t)$ and $\nu(t)$ via least squares [39, 40]. The left hand side of (6) is available from scaling the equivalent injection $\bar{v}(t)$, obtained via low-pass filtering according to (39). To avoid the effect of any phase lag associated with the filter, the terms on the right hand side of (6) are also subjected to the same filter

$$\tau\dot{\bar{Y}} = -\bar{Y} + Y(L),\ \bar{Y}(0) = 0. \tag{41}$$

The proposed estimation approach is to first estimate the equivalent injection v_{eq}, then, for the left and right hand of (6), a low-pass filtering algorithm is simultaneously applied to both the equivalent injection v_{eq} in (39) and the measured cantilever oscillation $Y(L)$ in (41) to obtain a filtered version of the estimated shear-force and the tip velocity (see for instance [39, 40]). After the force is obtained, the viscous and elastic constants can be estimated based on (6) as:

$$\hat{f}(t) = -\nu\frac{\partial\bar{Y}}{\partial t}(t) - \kappa\bar{Y}(t) \tag{42}$$

A benefit of using the filter in (41) is that $\frac{\partial \bar{Y}}{\partial t}$ can be constructed from the right hand of (41), and therefore measured knowledge of $\frac{\partial \bar{Y}}{\partial t}$ is not required. Recursive least squares procedures can then be used to estimate κ and ν [39].

5. Experimental Set Up

The VOC is made of silicon nitride and was specially designed and manufactured in Bristol (NuNano, Bristol, UK, www.nunano.com). There are three different sizes of ultra-soft cantilevers on a single VOC chip (approx. 2.3mm x 1.3mm). In the results which follow, the middle sized VOC was used for observing the viscoelastic response of the VOC tip in the ordered water layers. The dimensions of the VOC are $L = 28\mu$m (length) by 2μm (width) by 0.2μm (thickness) with a Young's Modulus of $E = 210 \cdot 10^9 \frac{kg}{m^{-1}s^{-2}}$. This yields a very soft spring constant of 0.038N/m in the horizontal direction with a first resonant mode at a frequency of approximately 350kHz. The VOC bottom tip is pointed over a length of 0.5μm.

The VOC chip is oriented in a direction perpendicular to the surface and is securely glued onto the cantilever base. In order to excite the VOC, a thin dither piezo actuator (Physik Instrument (PI), PL088.31) is attached under the cantilever base (see Fig. 2 for a principal overview). The whole VOC unit is rigidly mounted on a large piezo actuator (PI, P-885.11) for controlling the gap between the cover-slip/sample surface and the tip of the VOC (i.e. the Z-axis vertical height). A specifically designed high-speed nano-positioning stage tightly holds this quartz cover-slip (thickness $< 130\mu m$), which carries the specimen. This high speed X-Y stage is rigidly placed on top of a slower commercial X-Y stage (Physik Instrumente (PI) P-734 with scan range of $100\mu m$). The nano-positioning stages control the position of the sample in the X- and the Y- directions when the VOPM is in scanning mode.

An evanescent field-based detection mechanism is adopted for the VOPM to observe the VOC tip amplitude (deflection) as well as the tip to surface/sample distance. The scattered beam reflected from the VOC tip is captured by the quadrant photo-detector. Note that the total light intensity of all photo-diode sectors (sum signal) gives a measure of the absolute height from the surface of the cover-slip to the tip of the VOC.

Very importantly, the entire VOPM is bolted onto a vibration isolation table and covered with a heat insulated chamber to minimise temperature and humidity changes and external air vibrations during the operation.

To investigate the dynamics of the VOC in the proximity of the surface, a robust VOC Z-axis control unit is used that is able to maintain a constant tip-to-surface distance, using the Z-directed piezo-actuator. The sum of the scattered light detected at the quadrant photo-detector has been employed as the feedback signal for separation distance control. The dynamics of the VOPM in the Z-axis (including the piezo amplifier, piezo actuator, the VOC and the filters) have been identified prior to the design of a closed-loop controller. A robust $\mathcal{H}_\infty$ controller has been subsequently designed and implemented on the NI PXI-7854R FPGA board using LabVIEW with a control sample rate at 100kHz.

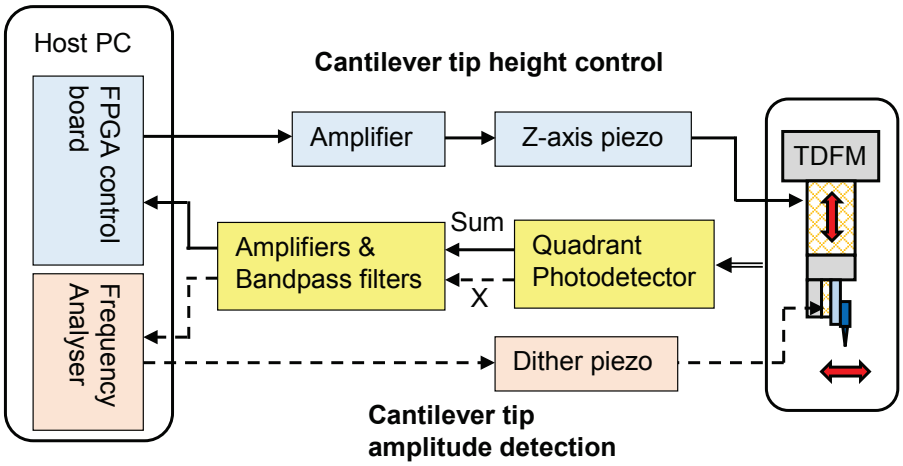

Figure 4: VOPM System Configuration for practical VOC-Analysis

6. Practical VOC-Analysis, Modelling and Observer Design

This section provides the vital detail for practical modelling, and subsequent design of the super-twisting observer. The process which has been followed is *a*) swept-sine data collection; *b*) swept-sine data calibration step 1 (relative magnitude); *c*) model fitting and data calibration (absolute magnitude); *d*) observer parameter design. The process has been very carefully devised so as to practically parametrize the model of (11)-(12) which infers the estimator parameter choice.

During the experiments a room temperature of 18.5°C and 53% humidity were maintained. Fig. 4 depicts the simplified VOPM system configuration for this VOC-analysis experiment. This system is composed of two modules; the cantilever tip amplitude detection unit with the cantilever tip height control unit and the frequency processing unit for analysis of the horizontal cantilever beam dynamics resulting from the dither piezo excitation at the top of the cantilever. For this, the National Instruments (NI) waveform generator (PXI-5421) and the NI digitiser (PXI-5122) were used to form a high-speed frequency analyzer.

6.1. Data collection

A swept sine wave with a constant amplitude can be generated from the waveform generator to excite the VOC. The tip response of the VOC is captured from the quadrant photo-detector after processing through a band-pass filter to remove unnecessary noise and offsets. In this test, the cutoff frequency for the high-pass filter and the low-pass filter are set as 1kHz and 500kHz, respectively. The input and output data are collected at a 10MHz sample rate and processed in real-time to compute its frequency response. At the same time, the VOC tip to the surface distance is required to remain at a constant height above the quartz glass slide for a measurement cycle. With each measurement cycle, the robust VOC Z-axis control is used to bring the VOC tip closer to the glass slide for measuring the next frequency response.

Initially, the VOC was positioned well above the thin ordered water layers (see inset of Fig. 2) so that the tip amplitude of the VOC is at a maximum (i.e. no shear force is acting on the VOC). From preliminary tests, the first mode resonant frequency of the VOC was established to be 352.75kHz. Therefore, a swept sine frequency range of 335kHz to 375kHz was chosen to study the dynamic behaviour of the VOC around its resonant frequency. The swept sine wave with a constant amplitude of 0.8nm was applied to the dither piezo actuator to excite the root of the VOC. The input (the excitation at the base of the VOC) and the output (the VOC tip amplitude) signals were acquired at a rate of 250Hz and the corresponding frequency responses (gain and phase) were computed while maintaining a constant separation distance between the tip and the surface. When the swept sine wave completes one full cycle (i.e. from 335kHz to 375kHz), the separation distance was decreased by 0.5 nm and the same process repeated until the tip contacted the sample or the cover-slip surface. In ambient conditions, the ordered water layers cause a shear force at the tip of the VOC. The oscillation amplitude of the

VOC decreases as the tip approaches the sample/cover-slip surface. This is due primarily to the increase of the tip contact surface area in relation to the ordered water layers, i.e. the depth of the tip within the ordered water layers – the greater the contact area the larger the shear force. At the end of this test, a number of bode plots at different heights were obtained.

6.2. First Data Calibration Step

The frequency response and the time-series data obtained from the tests must be properly calibrated before the unknown shear force estimation process takes place. Here, two calibration steps are described: namely, the sensor-based and the model matching-based calibrations. Usually, the evanescent field light strength (and subsequently the quadrant photo-detector signal) have an inversely-proportional (or exponentially decreasing) relationship in terms of quartz glass to VOC tip distance. Hence, the VOC oscillation signal captured from the photo detector depends not only on the shear force but also on this phenomenon (i.e. decreasing in magnitude with the decrease of the evanescent field light strength). Consequently the measured VOC amplitude (output) signal must be properly re-scaled in order to appropriately compare signals at different heights. However, the sensor property of the photo-detector in close proximity to the surface of the cover-slip (up to 10nm) can be treated as linear. Therefore, the following pre-scaling is applied to the VOC output signal:

$$y_i'[V] = \frac{S_1}{S_i} \times x_i[V] \tag{43}$$

for $i = 1 \ldots 22$. (Note that the subscript i corresponds to the data set number. Specifically $i = 1$ corresponds to the data collected closest to the surface and $i = 22$ is associated with the data farthest away from the surface.) In (43), x_i is the raw (unscaled) VOC output signal as a voltage, y_i' is the pre-scaled VOC output signal, and S_i is the total light intensity (sum signal) of the photodetector.

The frequency responses are now in the correct order and have the correct relative gain. There are several overlapped responses and so several distinct responses are extracted in Fig. 5 for clarity. The peak amplitude and the 90 degrees phase-lag are clearly seen at the VOC resonant frequency of 352.75kHz. It is also interesting to see the overall consistent phase gradient behaviour across the measured frequency range. It is important to note the drop in gain when the sample-to-tip distance decreases. This can be

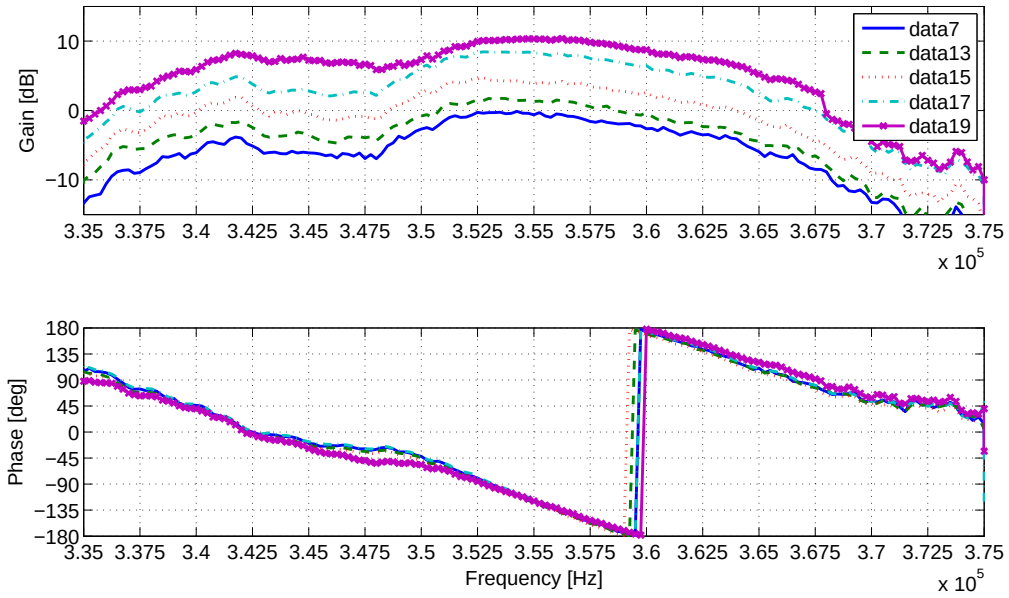

Figure 5: Frequency responses (bode plots) of the VOC at different sample-to-tip distances

explained by the VOC tip successively entering the ordered water molecules layer by layer causing the shear force effects to increase. In fact, for zero sample-to-tip distance, the tip oscillation is effectively zero for an excited cantilever at 352.75kHz.[5] The absolute gain of the frequency responses in Fig. 5 now needs to be determined in the final calibration step.

6.3. Modelling and final calibration

The absolute gain of the measured frequency responses needs to be recovered so that the cantilever excitation amplitude measured in nm relates to the VOC tip amplitude also measured in nm. The theoretical VOC model $\tilde{G}_u(s)$ from (12) in Section 3.1 and an actual data set (away from the ordered water layers), have to be compared in the frequency domain to identify a scale factor to match their gain responses. At low frequencies, where the phase

[5]The frequency response measurement at the correct resonant point is non-trivial and a conclusive proof for testing the correct structural modal flexibility is by the described amplitude test.

values are close to zero, the magnitude of the frequency response of $\tilde{G}_u(s)$ from (12) corresponds to unity (see Fig. 3). At the excitation signal frequency, the magnitude of the measured frequency response is equal to the magnitude of the transfer function of the approximate models in (11) and (12), which helps to calculate the scaling factor.

Fig. 6 shows the comparative plots of the frequency responses. In particular, the practically measured phase change $\frac{\partial \phi}{\partial \omega}$ has been used to find the damping coefficient ζ_0 in (12). The assumption $H_4(s)|_{s=jw_0} \approx 1$ (21) and $\angle(s+a_0)(s-a_1)|_{s=jw_0} \approx 0$ allows the use of the well-known relationship in second order systems,

$$\frac{\partial \phi(s=jw_0)}{\partial \omega} = -\frac{1}{\omega_0 \zeta_0} \tag{44}$$

to compute the damping from Fig. 6. Note that the phase response data and its gradient with respect to frequency is fully consistent across the measured region (see Figures 5 and 6). This allows the use of the arguments from equations (22) to adjust the internal damping coefficient α in (1) to satisfy the magnitude constraint for $|\tilde{G}_f(\cdot)|$. This automatically fixes the magnitude of $G_u(L,s)$ in (8) and therefore allows the computation of parameters in the rational transfer function $\tilde{G}_u$ in (12).[6] Hence, from ζ_0, it is subsequently possible to compute the rational transfer functions H_i (i=1,2,3,4) as discussed in Section 3.1.

The measured frequency response has to match the amplitude of $G_u(L,s)$ (8). Hence, a scale factor K_a is obtained. Thus, the final calibration step is carried out as:

$$y_i[nm] = K_a \times y_i'[V] \tag{45}$$

where y_i is the scaled VOC output signal in nm and y' is the pre-scaled VOC output signal.

Note that the input excitation signal applied at the fixed end of the VOC, u' is simply calibrated as:

$$u[nm] = 22[nm/V] \times u_i'[V] \tag{46}$$

[6]Note that an alternative approach was also considered which was to measure $G_u(s)$ at low frequency as it has to correspond to unity. Such low frequency measurements were found to be impractical to obtain. Hence, it was necessary to initially settle the damping coefficient ζ_0 in (13) from the practically measured phase change and then the amplitude of $G_f(L,s)$ and $G_u(L,s)$.

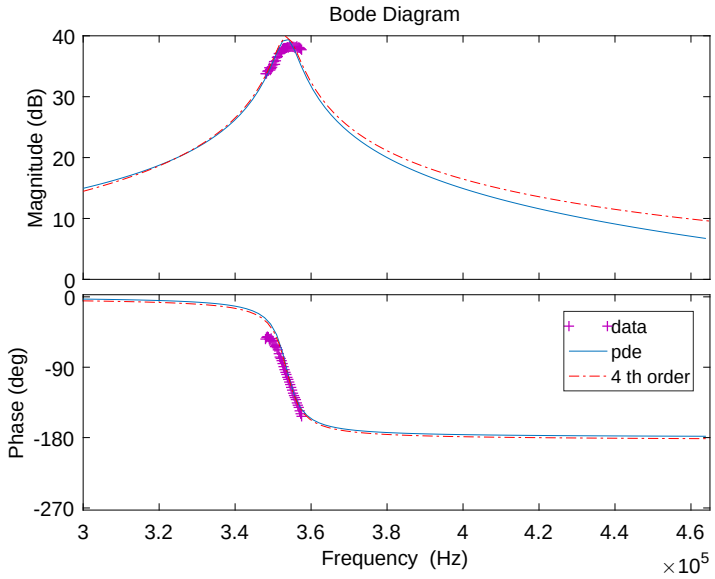

Figure 6: Comparison of the theoretical and the actual VOC responses away from the ordered water layers

where u is the calibrated signal in nm and u' is the raw data recorded as a voltage. The value 22 [nm/V] was obtained from the data sheet of the piezo actuator.

Following all the steps in Section 3.1 leads to the following parameters for the transfer functions $H_1(s)$, $H_2(s)$, $H_3(s)$ and $H_4(s)$ (11)-(16):

$$\begin{aligned}
&\omega_0 = 2 \cdot \pi \cdot 352.75kHz,\ \zeta_0 = 0.008454,\ a_0 = 2.866 \cdot 10^6,\ a_1 = 2.81 \cdot 10^6,\\
&\omega_1 = 1.55 \cdot 10^6,\ \zeta_1 = 0.0346,\\
&\omega_2 = 2 \cdot \pi \cdot 2.215 \cdot 10^6,\ \zeta_2 = 0.0562,\ a_2 = 22.348 \cdot 10^6,\ a_3 = 19.382 \cdot 10^6.
\end{aligned} \tag{47}$$

The next section will address the unknown shear force estimation problem using the calibrated input u and the output y of the VOC.

6.4. Super-Twisting Observer Design

In the state-space realizations of the filters and the observer in Section 4, balancing using the Matlab function 'balreal' has been employed to try to recover reasonably well-conditioned state-space matrices. During processing

the nonlinear injection signal v from the observer and the measured tip position $Y(L)$ are processed through identical low-pass filters (39)-(41), with $\tau = 1/500000$, to extract the filtered equivalent injection v_{eq}, the filtered $\bar{Y}(L)$ and the filtered velocity $\dot{\bar{Y}}(L)$ for the least squares calculations. Considering that the excitation is at $\omega = 2 \cdot \pi \cdot 352.75kHz$, the parameter choice $\tau = 1/500000$ provides sufficient gain while also attenuating some of the noise at higher frequency. The parameters for the observer (32) were chosen as $k_1 = 10^{11}$ and $k_2 = 1.1 \times 10^{19}$. These were achieved by off-line tuning based on the linear cantilever model and with known "unknown inputs". The off-line parameter choice was iteratively conducted to satisfy the conditions of [19, 37], e.g. (37), while keeping the gains small enough to avoid numerical overflow and retain numerical stability. The scheme to estimate the shear force and the parameters in the shear force model in (6) is shown in Fig. 7.

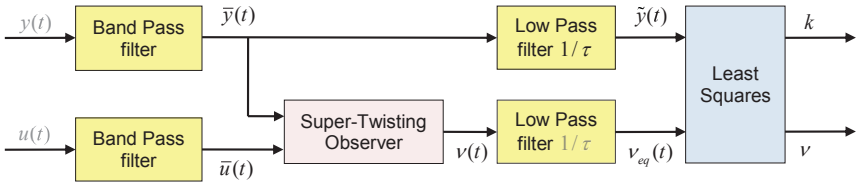

Figure 7: Signal processing schematic

7. Experimental Results

This section describes the experimental results for the observer demonstrating its capacity to estimate the shear force at the tip considering a tip excitation at 352.75kHz. The scaled data (u and y) has first been band-pass filtered to emphasize the frequency range 352.75kHz (and to remove noise).

Fourteen data sets were selected from the original 22 with tip-to-surface distances corresponding to 1.5 nm to 8 nm respectively. The top of the cantilever was excited at its resonance frequency. The amplitude of the excitation signal was 1.8 nm.

7.1. Tip motion

A typical time response of the tip motion is shown in the upper frame of Fig. 8. The root-mean-square (RMS) value of the tip oscillation y is plotted as a function of tip cover-slip distance in Fig. 9. It is evident that the

tip oscillation amplitude decreases as the proximity of the cantilever to the cover-slip increases. Fig. 9 shows some small exceptions in this monotonic behaviour which is expected due to the discontinuous, lattice-like structure of the ordered layer above the cover-slip [10], creating partial but also small discontinuities in the graph.

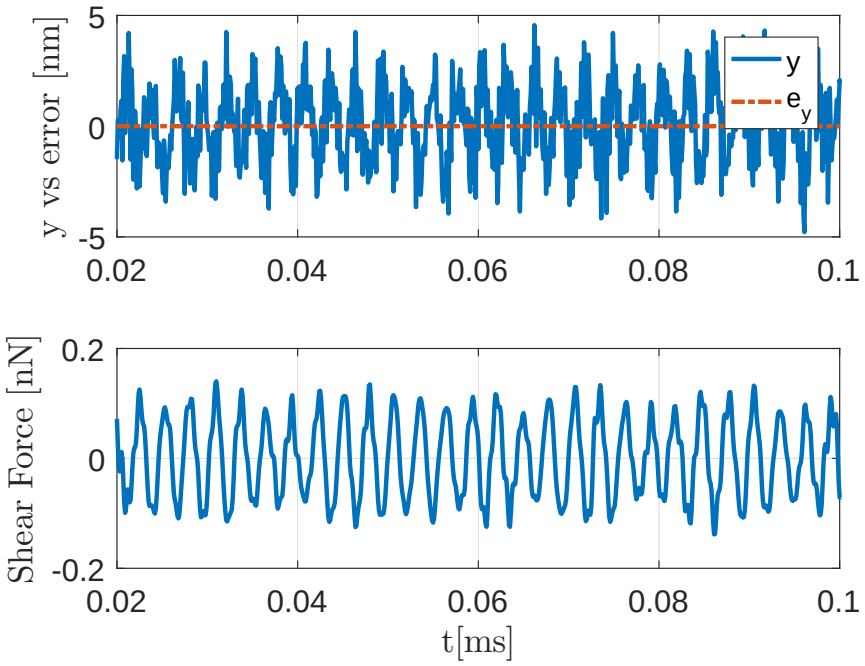

Figure 8: Output signal y, output estimation error e_y, and estimate of shear force for data with a 4.5 nm distance between the cantilever tip and cover-slide

7.2. Shear force Estimation

The measured tip position for this data set is shown in Fig. 8, which also provides the output estimation for e_y. The error signal is nine orders of magnitude smaller than the tip position signals which indicates a sliding motion is taking place. Fig. 8 shows the shear force estimates $\hat{f}(t)$ for the data set with a 4.5 nm distance. All the shear force estimates appear as (noise affected) sinusoidal signals with the same frequency as the excitation signal $u(t)$. (These signals are quite typical, the other signals are not shown

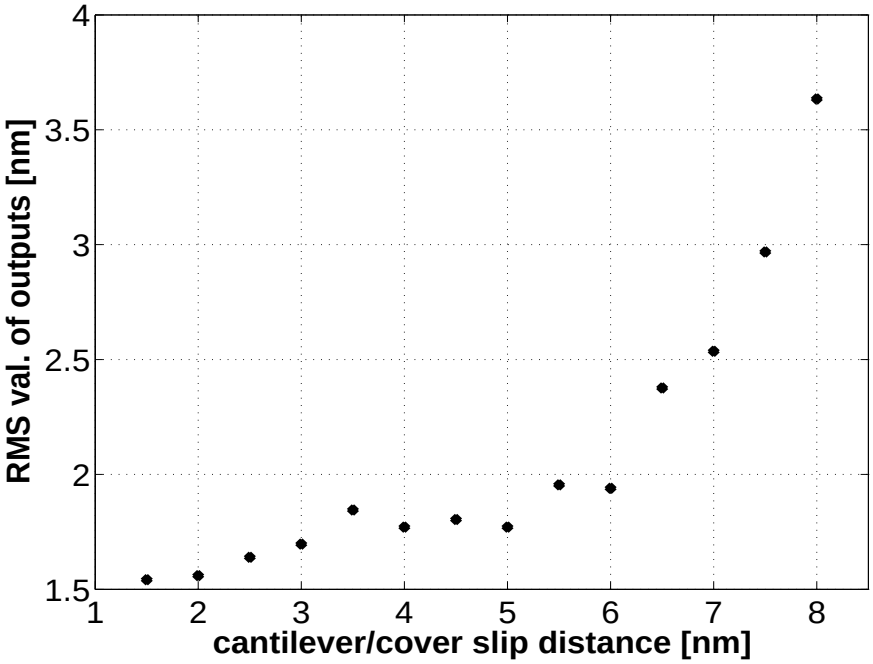

Figure 9: RMS value of output signal y as a function of cantilever to cover-slip distance

here for reasons of space.)[7] It is also clear that the shear force corresponding to the data set with the smallest distance to the cover-slip exhibits the largest amplitude, implying interaction with the ordered water layers, as observed in Fig. 10. This result within a relative distance range of [1.5, 8] nm and RMS magnitudes below 0.1 nN confirms earlier measurements [10]. Antognozzi et al. [10] measured within the range of [0.8, 2] nm, where our work overlaps within the range of [1.5,2] nm; there it fits the magnitude and the general trend of previous data. Thus, the results obtained from the experiments for the suggested estimator are fully consistent with previous work [10], while overall the detection of the shear forces remains an area of research. The important difference of the results here compared to [10] is that the estimation

[7]It is in principle possible to design a mixed-sensitivity H_∞-estimator [24] which has an overall order of 5 and provides similar performance. The mixed sensitivity dynamics for design have to be chosen to reflect the second order system dynamics of (28)-(29) together with two weights each limiting the frequency range of the estimation error and the estimated signal. Evidently, such a high order estimator creates additional challenges.

scheme is easily incorporated into a fully automated scanning regime.

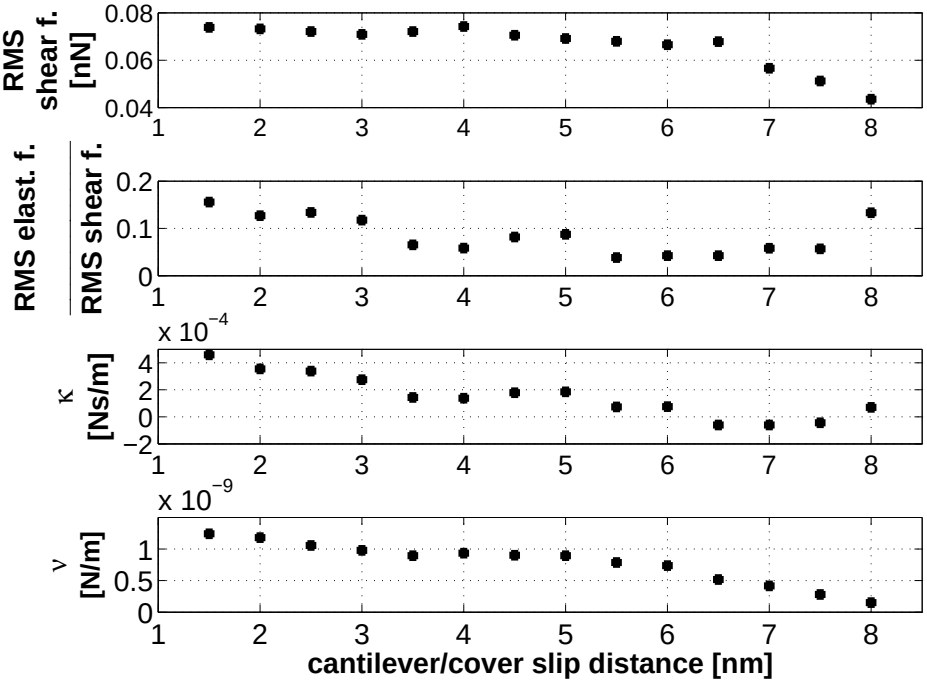

Figure 10: Shear force characteristics as a function of cantilever to cover-slip distance: a) RMS value of shear force, b) RMS value of elastic force in relation to RMS value of shear force, c&d) Estimates of κ and ν

7.3. Shear force components and material parameters

It is now possible to estimate the elastic and viscous components in (42). It is interesting to see (Fig. 10) that the elastic component $-\kappa\bar{Y}(t)$ has only a small contribution to the shear force. The RMS of the elastic component is less than 16% of the RMS value of the shear force, i.e. less than 3% in terms of overall energy/power. The contribution of the elastic force is significantly lower when the cantilever cover-slip distance increases. (Note that the shear force itself is rather small when the distance between cantilever and cover-slip has increased to 8 nm.) Thus, one can expect a higher level of inaccuracy in the estimate of the elastic forces in particular for larger distances between cantilever and cover-slip.

It is therefore evident that the estimation of the elastic forces and the relevant elastic constant is not of acceptable quality for large cantilever cover-slip

distances where the shear force itself is small and the estimated contribution of the elastic component small (see Fig. 10). The negative values for the estimated κ in that region are clearly erroneous and can be attributed to the large effect of noise. For decreasing cantilever cover-slip distance, the elastic component and the relevant constant κ is increasing and positive, which also points to an increase of the shear force. The viscous term $-\nu\frac{\partial \bar{Y}}{\partial t}(t)$ shows also an increase in constant ν and subsequently also in terms of magnitude (Fig. 10). Nevertheless, the elastic component in contrast to the viscous component has in this case minimal contribution to the characteristics of the ordered water layer. This also confirms recent results from [10], where the magnitude of the elastic shear force component in the relative distance range above 1 nm significantly drops.

8. Conclusion

This paper has described a novel scheme to reconstruct the *unmeasurable* shear forces acting on the tip of a vertically oriented cantilever, based on a super-twisting sliding mode observer. The response of the tip to such forces is a vital component of Bristol University's Vertically Oriented Probe Microscope and is the key mechanism which is used to infer the distance between the tip and the specimen surface. The shear forces which result from the fluid/tip interaction increase with increasing proximity of the tip to the surface of the specimen under investigation. Consequently, knowledge of the shear forces indirectly measures the proximity of the cantilever tip to the specimen. In this paper, by exploiting an LTI system representation of the cantilever, the problem of shear force estimation is formulated as an Unknown Input Observer problem. The super-twisting observer is designed from a 2nd order LTI system which relates the unknown input shear force to the measured tip displacement. This system is relative degree two and so classical linear unknown input observers cannot be used in this situation – hence the use of a bespoke super-twisting formulation. The paper has described the physical set up of the VOPM at Bristol and the mechanism by which the amplitude of oscillation of the cantilever can be measured and then calibrated. For this calibration, the analytical cantilever model is vital, leading to a parameter identification based calibration process. The results from a series of tests during which the cantilever is suspended at different heights above the glass slide demonstrate the potential of the system to estimate shear forces. These outcomes confirm, using both the frequency

and also the time responses, the increasing influence of the viscous forces resulting from the cantilever interacting with the ordered water layer. This is reflected in the decrease in amplitude in both cases. Moreover, no significant shift in resonance frequency is detected in the frequency response, which also indicates the low influence of the elastic forces. The combined information of shear forces, shear force components and material parameters can help the investigation, in particular, of bio-specimen. Overall, the problem of shear force estimation/measurement is still unresolved but the understanding of the shearforce and their components can provide significant impact on biomedical research such as in cancer treatment.

Acknowledgement

This research was supported under the EPSRC grants EP/I034882/1 & EP/I034831/1.

Appendix - Notation

E	Young's modulus of the cantilever
I	the second moment of area
A_s	the cross-sectional area of the cantilever
α	the internal damping constant of the cantilever
ρ	the cantilever density
γ	the damping coefficient of the cantilever
w	cantilever width
L	cantilever length
Y	the transverse displacement at any point along the probe
ζ	any position along the probe axis
d_0	the frequency of the sinusoidal excitation to the cantilever
ω	the amplitude of the sinusoidal excitation to the cantilever
u	the excitation applied to the cantilever's top
f	the interaction shear-force between the cantilever tip and the specimen
ν	dissipative constant of the shear-force interaction
κ	elastic constant of the shear-force interaction
$Y(L,s)$	the Laplace transformation of the cantilever tip oscillation where $\zeta = L$

$U(s)$	the Laplace transformation of the cantilever excitation
$F(s)$	the Laplace transformation of the interaction shear-force
G_u	transfer function from $F(s)$ to $Y(L,s)$
G_f	transfer function from $U(s)$ to $Y(L,s)$
$\tilde{G}_u$	fitted transfer function from $F(s)$ to $Y(L,s)$
$\tilde{G}_f$	fitted transfer function from $U(s)$ to $Y(L,s)$
$H_{i=1,..,4}(s)$	2nd order transfer functions to construct $\tilde{G}_u$ and $\tilde{G}_f$
$a_{i=0,..,3}$	positive parameters to construct $H_{i=1,..,4}(s)$
$\omega_{i=0,..,3}$	natural frequencies associated with $H_{i=1,..,4}(s)$
$\zeta_{i=0,..,3}$	damping ratios associated with $H_{i=1,..,4}(s)$
$\tilde{u}$	filtered u by H_4
$\tilde{f}$	filtered f by H_3
y	the cantilever tip (deflection) oscillation
x	an abstract vector used for establishing a state-space representation between $\tilde{u}$, $\tilde{f}$ and $y(t)$
$k_{i=1,2}$	designed gains in the super-twisting observer
v_{eq}	the equivalent injection of the super-twisting obverse
$\bar{v}$	low-pass filtered v_{eq}
$\tilde{f}$	estimated shear-force
$\bar{Y}$	low-pass filtered cantilever tip oscillation

References

[1] G. Binnig, C. F. Quate, C. Gerber, Atomic force microscope, Physical review letters 56 (9) (1986) 930 (1986).

[2] K. A. Ramirez-Aguilar, K. L. Rowlen, Tip characterization from afm images of nanometric spherical particles, Langmuir 14 (9) (1998) 2562–2566 (1998).

[3] R. S. M. Mrinalini, R. Sriramshankar, G. Jayanth, Direct measurement of three-dimensional forces in atomic force microscopy, IEEE/ASME Transactions on Mechatronics 20 (5) (2015) 2184–2193 (2015).

[4] S. N. Magonov, M.-H. Whangbo, Surface analysis with STM and AFM: experimental and theoretical aspects of image analysis, John Wiley & Sons, 2008 (2008).

[5] K. K. Leang, S. Devasia, Feedback-linearized inverse feedforward for creep, hysteresis, and vibration compensation in afm piezoactuators,

IEEE Transactions on Control Systems Technology 15 (5) (2007) 927–935 (2007).

[6] D. Y. Abramovitch, S. B. Andersson, L. Y. Pao, G. Schitter, A tutorial on the mechanisms, dynamics, and control of atomic force microscopes, in: 2007 American Control Conference, IEEE, 2007, pp. 3488–3502 (2007).

[7] N. A. Burnham, R. J. Colton, Measuring the nanomechanical properties and surface forces of materials using an atomic force microscope, Journal of Vacuum Science & Technology A: Vacuum, Surfaces, and Films 7 (4) (1989) 2906–2913 (1989).

[8] M. Antognozzi, A. Ulcinas, L. Picco, S. Simpson, P. Heard, M. Szczelkun, B. Brenner, M. Miles, A new detection system for extremely small vertically mounted cantilevers, Nanotechnology 19 (38) (2008) 384002 (2008).

[9] R. Harniman, J. Vicary, J. Hörber, L. Picco, M. Miles, M. Antognozzi, Methods for imaging dna in liquid with lateral molecular-force microscopy, Nanotechnology 23 (8) (2012) 085703 (2012).

[10] M. Antognozzi, A. Humphris, M. Miles, Observation of molecular layering in a confined water film and study of the layers viscoelastic properties, Applied Physics Letters 78 (3) (2001) 300–302 (2001).

[11] P. James, M. Antognozzi, J. Tamayo, T. McMaster, J. Newton, M. Miles, Interpretation of contrast in tapping mode afm and shear force microscopy. a study of nafion, Langmuir 17 (2) (2001) 349–360 (2001).

[12] R. Brunner, O. Marti, O. Hollricher, Influence of environmental conditions on shear–force distance control in near-field optical microscopy, Journal of Applied Physics 86 (12) (1999) 7100–7106 (1999).

[13] S. Davy, M. Spajer, D. Courjon, Influence of the water layer on the shear force damping in near-field microscopy, Applied physics letters 73 (18) (1998) 2594–2596 (1998).

[14] P. Sandoz, J.-M. Friedt, E. Carry, Vibration amplitude of a tip-loaded quartz tuning fork during shear force microscopy scanning, Review of Scientific Instruments 79 (8) (2008) 086102 (2008).

[15] K.-D. Park, D. J. Park, S. G. Lee, G. Choi, D.-S. Kim, C. C. Byeon, S. B. Choi, M. S. Jeong, Operation of a wet near-field scanning optical microscope in stable zones by minimizing the resonance change of tuning forks, Nanotechnology 25 (7) (2014) 075704 (2014).

[16] A. Labernadie, A. Bouissou, P. Delobelle, S. Balor, R. Voituriez, A. Proag, I. Fourquaux, C. Thibault, C. Vieu, R. Poincloux, et al., Protrusion force microscopy reveals oscillatory force generation and mechanosensing activity of human macrophage podosomes, Nature Communications 5 (2014) 5343 (2014).

[17] A. F. Payam, D. Martin-Jimenez, R. Garcia, Force reconstruction from tapping mode force microscopy experiments, Nanotechnology 26 (18) (2015) 185706 (2015).

[18] Y.-x. Ding, Y. Cheng, Q.-m. Sun, Y.-y. Zhang, K. You, Y.-l. Guo, D. Han, L. Geng, Mechanical characterization of cervical squamous carcinoma cells by atomic force microscopy at nanoscale, Medical Oncology 32 (3) (2015) 71 (2015).

[19] J. Davila, L. Fridman, A. Levant, Second-order sliding-mode observer for mechanical systems, IEEE transactions on automatic control 50 (11) (2005) 1785–1789 (2005).

[20] L. Fridman, Y. Shtessel, C. Edwards, X.-G. Yan, Higher-order sliding-mode observer for state estimation and input reconstruction in nonlinear systems, International Journal of Robust and Nonlinear Control: IFAC-Affiliated Journal 18 (4-5) (2008) 399–412 (2008).

[21] C. P. Tan, C. Edwards, Robust fault reconstruction in uncertain linear systems using multiple sliding mode observers in cascade, IEEE Transactions on Automatic Control 55 (4) (2010) 855–867 (2010).

[22] H. K. Khalil, L. Praly, High-gain observers in nonlinear feedback control, International Journal of Robust and Nonlinear Control 24 (6) (2014) 993–1015 (2014).

[23] P. Guerra, A. Valbuena, J. Querol-Audí, C. Silva, M. Castellanos, A. Rodríguez-Huete, D. Garriga, M. G. Mateu, N. Verdaguer, Structural basis for biologically relevant mechanical stiffening of a virus capsid by cavity-creating or spacefilling mutations, Scientific reports 7 (1) (2017) 4101 (2017).

[24] J. Stoustrup, H. Niemann, Fault estimation—a standard problem approach, International Journal of Robust and Nonlinear Control 12 (8) (2002) 649–673 (2002).

[25] G. Besançon, A. Voda, M. Alma, On observer-based estimation enhancement by parametric amplification in a weak force measurement device, in: 2008 47th IEEE Conference on Decision and Control, IEEE, 2008, pp. 5200–5205 (2008).

[26] T. De, P. Agarwal, D. R. Sahoo, M. V. Salapaka, Real-time detection of probe loss in atomic force microscopy, Applied physics letters 89 (13) (2006) 133119 (2006).

[27] T. Shiraishi, H. Fujimoto, High-speed atomic force microscope by surface topography observer, Japanese Journal of Applied Physics 51 (2R) (2012) 026602 (2012).

[28] Y. Fang, M. Feemster, D. Dawson, N. M. Jalili, Nonlinear control techniques for an atomic force microscope system, Journal of Control Theory and Applications 3 (1) (2005) 85–92 (2005).

[29] X. Xu, J. Melcher, A. Raman, Accurate force spectroscopy in tapping mode atomic force microscopy in liquids, Physical Review B 81 (3) (2010) 035407 (2010).

[30] T. Nguyen, T. Hatano, S. G. Khan, K. Zhang, C. Edwards, R. Harniman, S. C. Burgess, M. Antognozzi, M. Miles, G. Herrmann, Estimation of the shear force in transverse dynamic force microscopy using a sliding mode observer, AIP Advances 5 (9) (2015) 097157 (2015).

[31] M. Antognozzi, Investigation of the shear force contrast mechanism in transverse dynamic force microscopy., Ph.D. thesis, University of Bristol (2000).

[32] T. Nguyen-Tien, S. G. Khan, C. Edwards, G. Herrmann, R. Harniman, S. C. Burgess, M. Antognozzi, M. Miles, Shear force reconstruction in a vertically oriented probe microscope using a super-twisting observer, in: 52nd IEEE Conference on Decision and Control, IEEE, 2013, pp. 4266–4271 (2013).

[33] R. F. Curtain, H. Zwart, An introduction to infinite-dimensional linear systems theory, Vol. 21, Springer Science & Business Media, 2012 (2012).

[34] G. Balas, R. Chiang, A. Packard, M. Safonov, Robust control toolbox user's guide, The MathWorks Inc., 2012 (2012).

[35] M. Darouach, M. Zasadzinski, S. J. Xu, Full-order observers for linear systems with unknown inputs, IEEE transactions on automatic control 39 (3) (1994) 606–609 (1994).

[36] J. Chen, R. J. Patton, H.-Y. Zhang, Design of unknown input observers and robust fault detection filters, International Journal of control 63 (1) (1996) 85–105 (1996).

[37] A. Levant, Robust exact differentiation via sliding mode technique, Automatica 34 (3) (1998) 379–384 (1998).

[38] V. I. Utkin, Sliding modes in control and optimization, Springer Science & Business Media, 2013 (2013).

[39] S. Sastry, M. Bodson, Adaptive control: stability, convergence and robustness, Courier Corporation, 2011 (2011).

[40] J. Na, M. N. Mahyuddin, G. Herrmann, X. Ren, P. Barber, Robust adaptive finite-time parameter estimation and control for robotic systems, International Journal of Robust and Nonlinear Control 25 (16) (2015) 3045–3071 (2015).